SUPPLEMENTARY INFORMATION

Young probing fluorescence microscopy: Single-pixel imaging free of array-type actuators

YINGCHAO LI[1], JACO BOTHA[1], PATRICK KLINT[1], JADZE PRINCETON CASILANA NARAG[1], CARL EMIL SCHØIER KOVSTED[1], LASSE PÆRGÅRD KRISTIANSEN[1], NIELS BENT LARSEN[1], JONAS NYVOLD PEDERSEN[1], AND EMIL BOYE KROMANN[1,*]

[1]Department of Health Technology, Technical University of Denmark.
Ørsteds Plads 345C, 2800 Kgs. Lyngby, Denmark
** ebkro@dtu.dk*

Contents

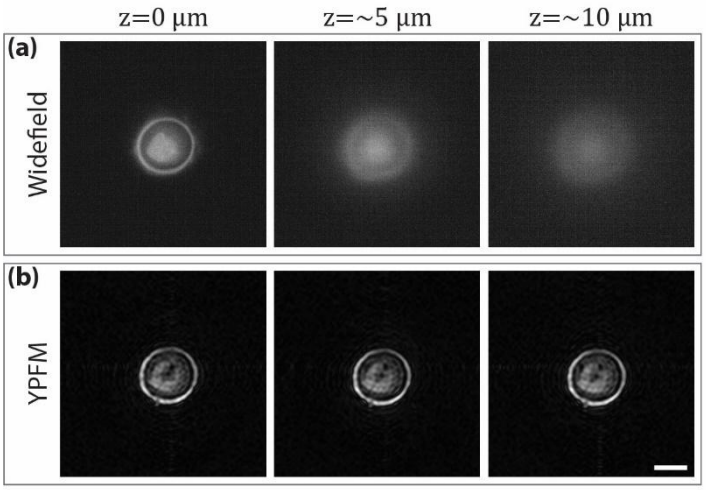

Supplementary Fig. 1 | Projection imaging captures the zone of adhesion in a CHO cell. a, Widefield images of fixed CHO cell labeled with Alexa Fluor 555 Phalloidin, captured at indicated position-offsets relative to the focal plane ($z = 0$). **b**, YPFM images of the same cell at the same positions as in (**a**), captured with the camera-proximal detector, $L = 52$ μm, $N = 35$. Notice that the YPFM images of the cell always capture actin distributed cortically along the cell membrane, consistent with suspended CHO cells[1] and the early formation of central stress fibers between the cell membrane and the nucleus in the zone of adhesion[2,3], regardless of sample positioning. Exc = 532 nm. Det = 585/65 nm. Scale bar = 10 μm.

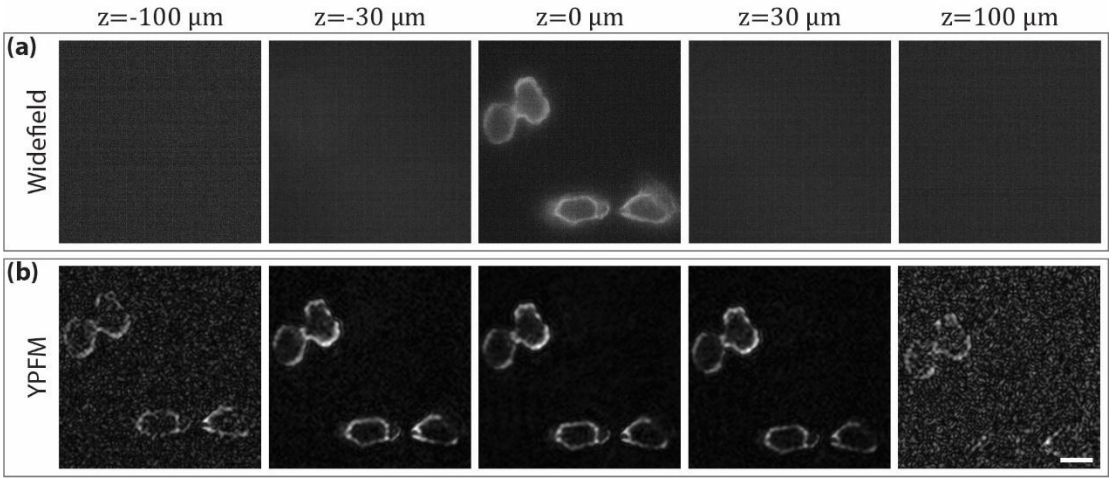

Supplementary Fig. 2 | Projection imaging at extreme position-offsets relative to the focal plane. **a**, Widefield images of fixed CHO cells labeled with Alexa Fluor 555 Phalloidin, captured at indicated position-offsets relative to the focal plane ($z = 0$). **b**, YPFM images of the same cells at the same positions as in (**a**), captured with the camera-proximal detector, $L = 52$ µm, $N = 35$. Exc = 532 nm. Det = 585/65 nm. Scale bar = 10 µm.

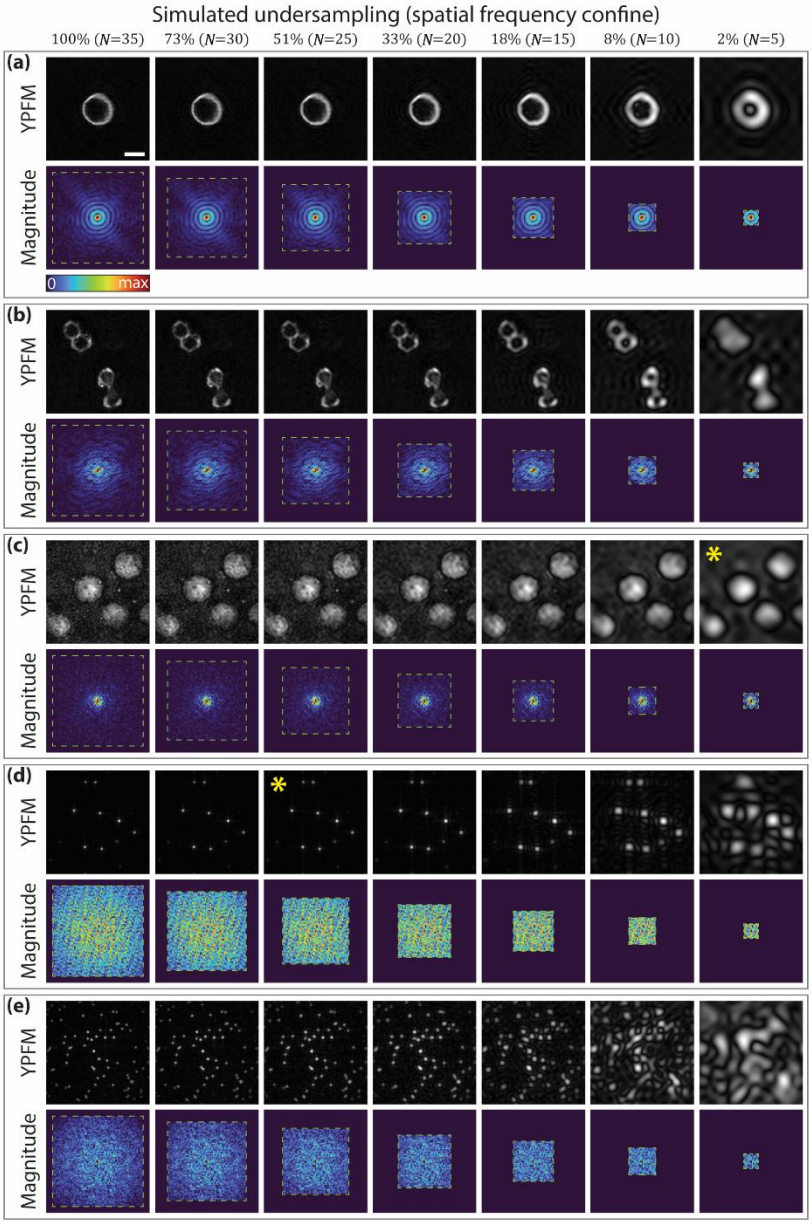

Supplementary Fig. 3 | YPFM is compatible with adaptive undersampling. Starting from fully sampled image data (left column), we simulate the corresponding image data that would be obtained if the spatial frequency confine (N) was reduced. The percentages indicated at the top of each column describe the proportion of Fourier coefficients that are *not* set to a value of zero. **a**, The CHO cell displayed in Fig. 3. **b**, The CHO cells displayed in Fig. 1a. **c**, The HEK-293 cells displayed in Fig. 1b. **d**, The fluorescent beads displayed in Fig. 1b. **e**, A monolayer of fluorescent beads, 1 μm diameter, not displayed elsewhere. Dashed green boxes outline the spatial frequency confine. Yellow asterisks indicate the two images that are merged as a two-color image in Fig. 1f. Exc = 532 nm and Det = 585/65 nm in (**a,b,d,e**). Exc = 488 nm and Det = 510/20 nm in **(c)**. Scale bar = 10 μm.

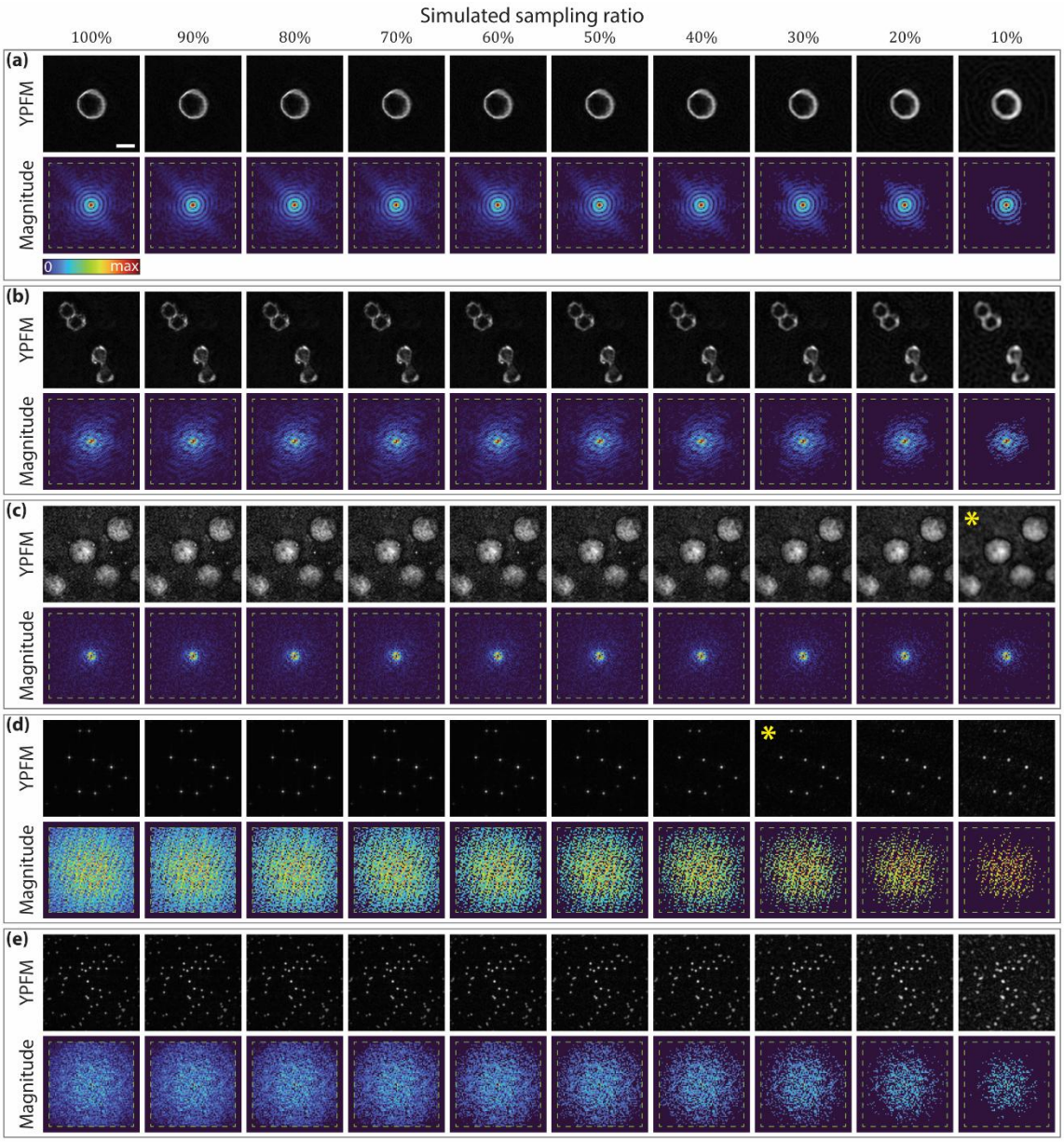

Supplementary Fig. 4 | YPFM is compatible with compressed sensing. Starting from fully sampled image data (left column), we simulate the corresponding image data that would be obtained if the least signal-rich Fourier coefficients were not measured. The simulated sampling ratios, indicated at the top of each column, describe the proportion of Fourier coefficients that are *not* set to a value of zero. **a**, The CHO cell displayed in Fig. 3. **b**, The CHO cells displayed in Fig. 1a. **c**, The HEK-293 cells displayed in Fig. 1b. **d**, The fluorescent beads displayed in Fig. 1b. **e**, A monolayer of fluorescent beads, 1 μm diameter, not displayed elsewhere. Dashed green boxes outline the spatial frequency confine. Yellow asterisks indicate the two images that are merged as a two-color image in Fig. 1g. Exc = 532 nm and det = 585/65 nm in (**a**,**b**,**d**,**e**). Exc = 488 nm and, det = 510/20 nm in **(c)**. Scale bar = 10 μm.

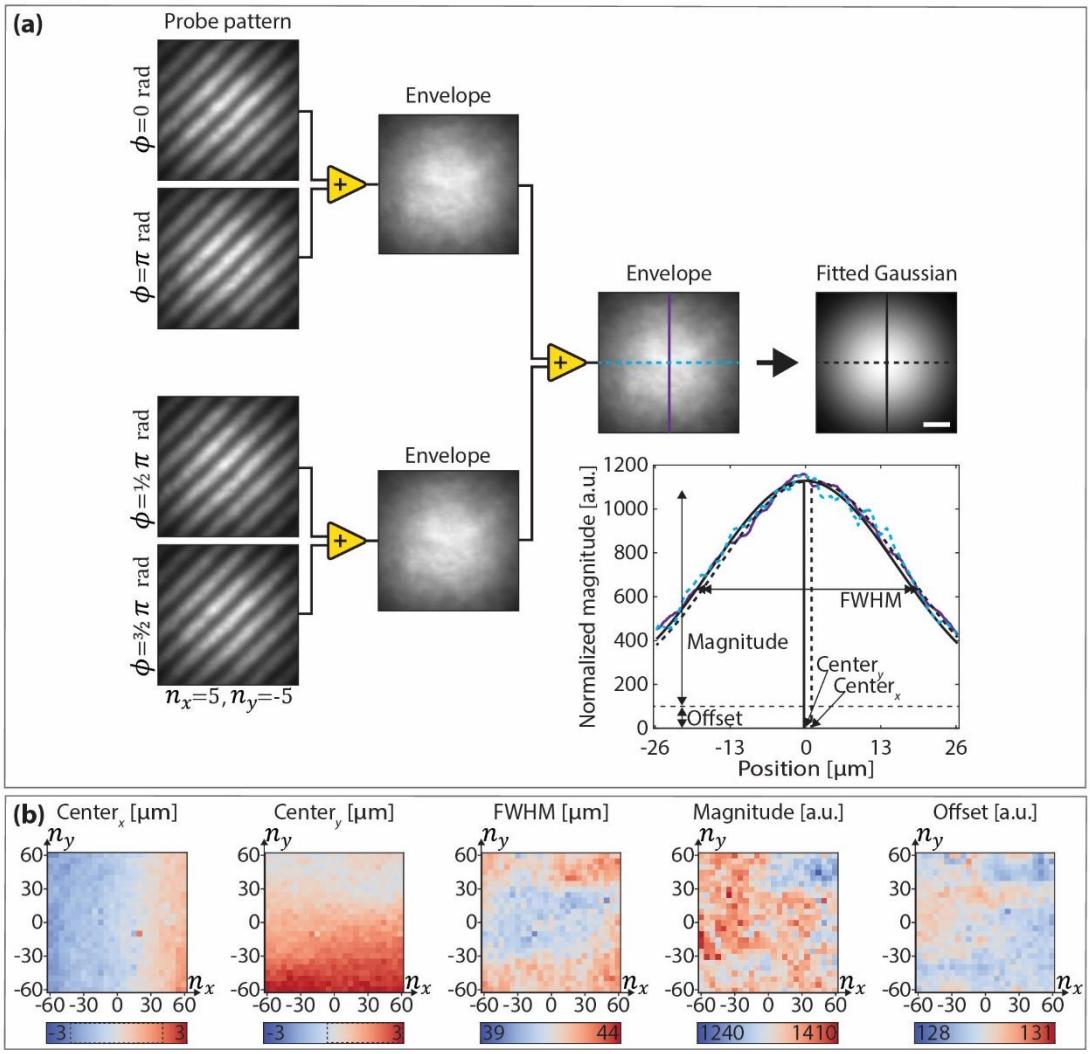

Supplementary Fig. 5 | Characterization of the quasi-Gaussian envelope function. **a**, Exemplification of how the quasi-Gaussian envelope function was measured as the summation (+) of probe patterns imaged with the camera. The black arrow denotes fitting of a 2D Gaussian function with five free parameters, as indicated with corresponding colors and line styles in the inset. **b**, Fitted parameters, as presented in (**a**), obtained from images of probe patterns with different spatial frequencies across a spatial frequency confine of $N = 60$. To help interpretation of plots for center$_x$ and center$_y$, we used identical colormap-ranges, when plotting these two parameter-estimates. Their actual dynamic ranges, [-1.95, 1.90] and [-0.36, 3.38], are indicated by dashed boxes inside their respective colorbars. Exc = 532 nm. Det = 585/65 nm. Scale bar = 10 µm.

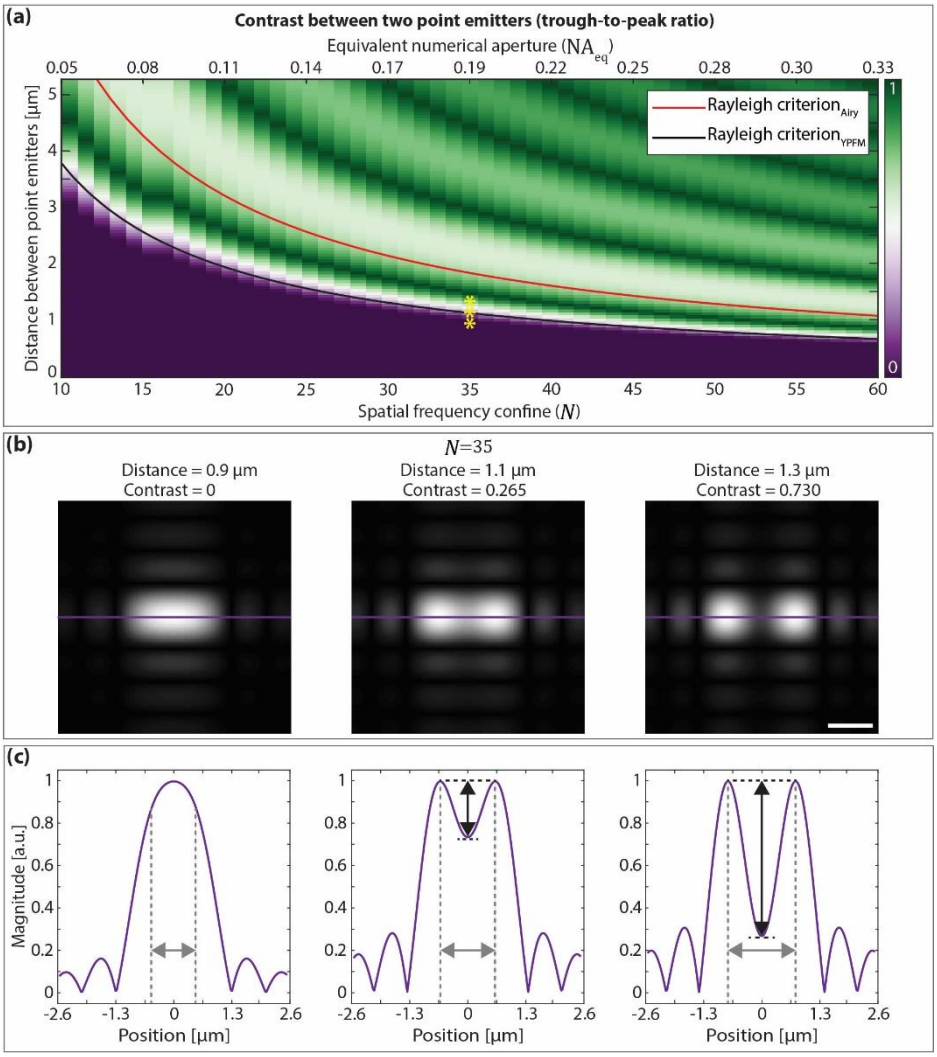

Supplementary Fig. 6 | Numerical simulations to describe imaging contrast/resolution. **a**, Numerical simulations of imaging contrast, which is also a measure of resolution in YPFM microscopy. The contrast quantifies how well we can distinguish two identical point emitters as a function of their separation distance and spatial frequency confine N. The contrast, ranging from 0 to 1, is computed as indicated in (**c**). The solid black line (subscript YPFM) indicates our interpretation of the Rayleigh resolution criterion (contrast ≥ 0.265) in the YPFM microscope, and the red line (subscript Airy) indicates the corresponding Rayleigh resolution criterion in a widefield microscope with equivalent numerical aperture (NA_{eq}). Yellow asterisks indicate datapoints associated with plots in (**b,c**). **b**, Representative simulated YPFM images of two identical point emitters separated by distances as indicated and imaged with a spatial frequency confine of $N = 35$. Scale bar = 1 μm. **c**, Signal profiles through emitters as indicated with solid purple lines in (**b**). Black arrows indicate estimated contrasts. Dashed gray lines indicate simulated positions of point emitters, and gray arrows indicate separation distances. The contrast derived from the central plots in (**b,c**) define, for YPFM, a Rayleigh-equivalent resolution of 1.1 μm for $N = 35$ and $NA_{eq} = 0.19$.

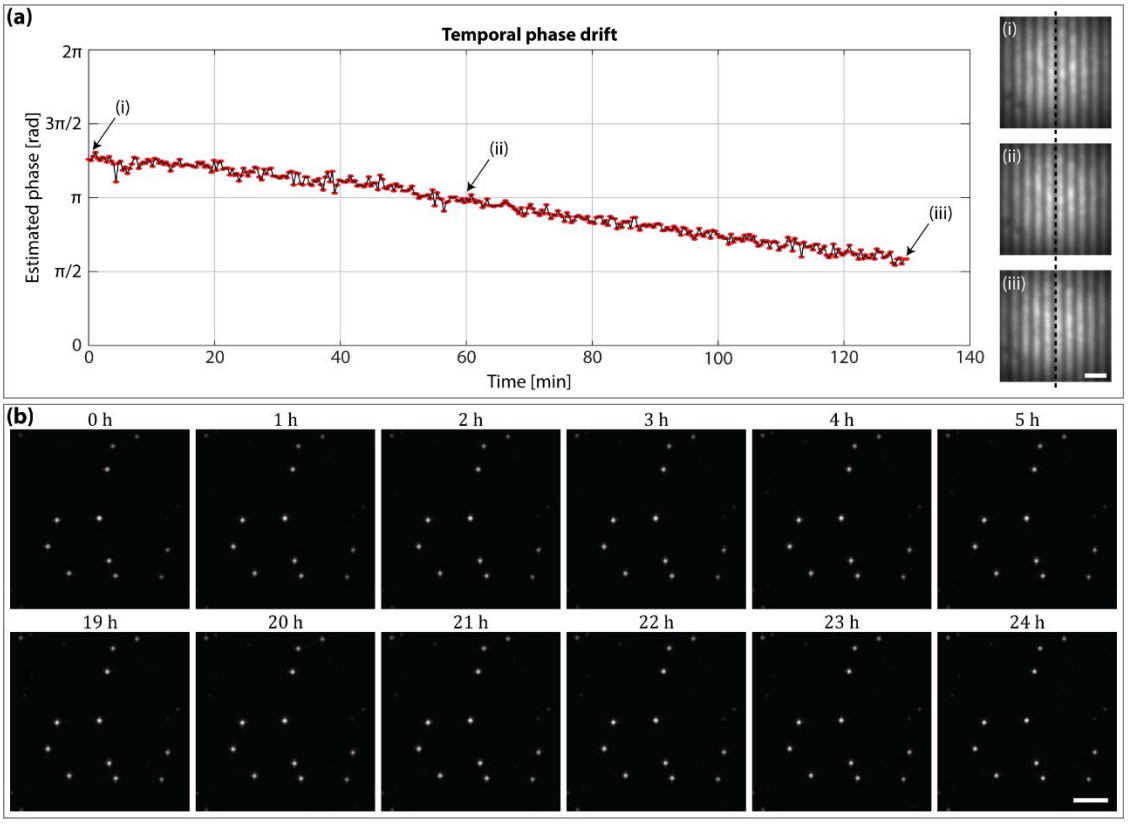

Supplementary Fig. 7 | YPFM is robust against long-term phase drift. **a**, Phase estimates obtained from widefield images of a probe pattern ($n_x = 10, n_y = 0$) imprinted onto a homogenously fluorescent sample (Alexa Fluor 568, dye in suspension). Images were captured with 20 s intervals, while keeping all acquisition settings constant. Insets (i)-(iii) display representative widefield images acquired at the correspondingly labeled timepoints. The vertical dashed black line transecting the insets is intended to make the temporal phase drift easier to observe. A phase drift of $>\pi/4$ rad h^{-1} is evident. **b**, A series of YPFM images of the same fluorescent beads (diameter = 1 µm) captured with the camera-proximal detector, $L = 52$ µm, $N = 35$. The YPFM images are near-identical across a time interval of 24 h. Exc = 532 nm. Det = 585/65 nm. Scale bars = 10 µm.

Supplementary Note 1
YPFM is compatible with compressed sensing

1.1 Sparse sampling within the spatial frequency confine

Compressed sensing covers a broad range of algorithms and mechanisms designed to prioritize measurement of those image constituents that provide most (useful) information to the image[4–6]. Compressed sensing strategies can harness *a priori* knowledge/assumptions about the structures being imaged and may also adaptively prioritize patterns during image data acquisition. As such, we may view compressed sensing strategies as *pre-* and *peri-* equivalents of *post*-acquisition image compression, with the added benefits of reducing sample exposure and image acquisition time. Historically, single-pixel imaging has been almost synonymous with compressed sensing. Indeed, Duarte *et al.* immediately demonstrated the application of compressed sensing in their initial demonstration of the single-pixel imaging concept[4]. Providing a full account of compressed sensing and how it may be applied in YPFM imaging is beyond the scope of this work. However, it would be nebulous to not discuss YPFM imaging in the context of compressed sensing and to show how compressed sensing can prove advantageous also for the YPFM variant of single-pixel imaging.

The direct compatibility with compressed sensing is one very attractive feature of single-pixel imaging – particularly for imaging applications (like live cell imaging) where phototoxicity is a concern. In this context the capacity of array-type actuators (like DMDs) to random access probe patterns is highly advantageous, i.e., the capacity to switch between arbitrary patterns, without following a predetermined order of patterns. Random access to probe patterns is maintained when we use sinusoidal patterns generated by non-binary beam deflection (Young probing). This is because the deflectors do not need to follow a rasterized path through Fourier space. Granted, the mechanical inertia of the galvanometric scanning mirrors used in the present YPFM microscope will limit the rate of switching and present a longer time to 'switch-and-settle' between patterns that are less similar (i.e., requiring farter travel across Fourier space) compared to 'switch-and-settle' times between very similar patterns located adjacent in Fourier space. Thus, our implementation with galvanometric scanning mirrors presents a disadvantage in the context of compressed sensing, when compared to DMD-based single-pixel imaging methods. This disadvantage may be addressed by introducing much faster (solid state/inertia-free) light modulators like acousto/electro-optic deflectors – although this will require careful compensation for the frequency and phase shifts that such instruments introduce. It may even be possible to use ultra-fast spectral scanning methods[7] – although spectral scanning is not readily geared to enable random access. We believe the work presented here represents a critical milestone on the path towards using solid-state or inertia-free deflection systems for single-pixel imaging, because we describe and solve challenges relating to aliasing and phase drift that are inherent to probing with patterns generated by interference of two independently steered beams (Young probing), i.e., challenges that would also exist for single-pixel imaging with fast beam-deflection systems.

To demonstrate the prospect of integrating compressed sensing with YPFM, we present **Supplementary Fig. 4**. Here, we simulate a simple variant of compressed sensing, which omits signal acquisition from the probe patterns that elicit the least signal. By tuning the number of omitted patterns, a content-adaptive algorithm can pick and effectuate a sampling ratio that presents an acceptable tradeoff between reduced image quality and improved imaging speed. For example, when choosing a sampling ratio of 40%, only 40% of the probe patterns (required to form a complete basis for image synthesis) are imprinted onto the sample. While this will improve imaging speed noticeably, the loss of image fidelity may still be negligible, as exemplified in **Supplementary Fig. 4**. We emphasize that **Supplementary Fig. 4** does not demonstrate real compressed sensing, as we reduced the sampling ratio 'artificially' through *post*-acquisition thresholding. We will not delve into methods and mechanisms necessary for identifying and actively omitting the low-signal probe patterns. Such methods are richly described in existing literature (e.g., [5,8]), and we expect that they may be readily adapted for YPFM.

Supplementary Note 2
Mathematical description of the probe patterns used in YPFM imaging

2.1 Definition of the complex electric field of a single electromagnetic plane wave propagating in 3D space

We use the complex representation of harmonic oscillations to define the electric field $\bar{E}_0$ of an electromagnetic plane wave propagating in three-dimensional (3D) space. In this definition, we omit time-dependence as well as the vectorial nature (polarization) of the electric field,

$$\bar{E}_0 = E_{00} \exp(\mathrm{i}\varphi_0) \tag{S1}$$

with

$$\varphi_0 = \mathbf{k} \cdot \mathbf{r} + \varphi_{00}, \tag{S2}$$

where the bar-symbol, '–', denotes complex notation with the imaginary unit 'i'. E_{00} is the amplitude of the plane wave, φ_0 is its phase, and φ_{00} is its initial phase. The symbol '·' denotes the scalar (dot) product between vectors. The three-dimensional vector $\mathbf{k}$ is the angular wave vector. The direction of $\mathbf{k}$ describes the propagation direction of the plane wave. The magnitude (k_λ) of $\mathbf{k}$ is the angular wave number and is defined by the wavelength of the electromagnetic radiation in vacuum (λ) and the refractive index (n_λ) of the propagation medium via the relation $|\mathbf{k}| = k_\lambda = 2\pi n_\lambda/\lambda$. The subscript ($\lambda$) is introduced to make a clear distinction from other variables (k_1, k_2, n_1, n_2), which are introduced later. The three-dimensional vector $\mathbf{r}$ is the position vector, which simply describes a position in 3D space. We describe 3D space as a 3D Cartesian coordinate system with unit vectors $\mathbf{e}_\mathrm{x}$, $\mathbf{e}_\mathrm{y}$ and $\mathbf{e}_\mathrm{z}$, and define the vectors $\mathbf{k}$ and $\mathbf{r}$ as

$$\mathbf{k} = k_\lambda \sin\theta \cos\beta\, \mathbf{e}_\mathrm{x} + k_\lambda \sin\theta \sin\beta\, \mathbf{e}_\mathrm{y} + k_\lambda \cos\theta\, \mathbf{e}_\mathrm{z}, \tag{S3}$$

$$\mathbf{r} = x\mathbf{e}_\mathrm{x} + y\mathbf{e}_\mathrm{y} + z\mathbf{e}_\mathrm{z}, \tag{S4}$$

where x, y and z are Cartesian coordinates, θ is the polar angle to the z-axis, and β is the azimuth to the x-axis in the xy-plane.

Omitting prefactors, e.g., the vacuum permittivity, we describe the intensity I of any complex electric field $\bar{E}$ at a given position $\mathbf{r}$ in 3D space by the direct proportionality,

$$I \propto \bar{E}\bar{E}^*, \tag{S5}$$

where $\bar{E}^*$ is the complex conjugate of $\bar{E}$.

2.2 Description of the interference pattern that arises upon superposition of two electromagnetic plane waves in 3D space

Using Eq. (S1) and Eq. (S2), we formulate from the two complex electric fields $\bar{E}_1$ and $\bar{E}_2$ two new electromagnetic plane waves propagating in the same 3D space,

$$\bar{E}_1 = E_{01} \exp(\mathrm{i}\varphi_1)\,, \tag{S6}$$

$$\bar{E}_2 = E_{02} \exp(\mathrm{i}\varphi_2)\,, \tag{S7}$$

with

$$\varphi_1 = \mathbf{k_1} \cdot \mathbf{r} + \varphi_{01}, \tag{S8}$$

$$\varphi_2 = \mathbf{k_2} \cdot \mathbf{r} + \varphi_{02}. \tag{S9}$$

The complex electric field $\bar{E}$ resulting from a superposition of these two electromagnetic plane waves is

$$\begin{aligned}\bar{E} &= \bar{E}_1 + \bar{E}_2 \\ &= E_{01}\exp(\mathrm{i}\varphi_1) + E_{02}\exp(\mathrm{i}\varphi_2).\end{aligned} \tag{S10}$$

By substituting Eq. (S10) into Eq. (S5) and then rewriting using Euler's formula, we obtain an expression for the intensity I of the electric field $\bar{E}$

$$\begin{aligned}I &\propto \bar{E}\bar{E}^* \\ &= [E_{01}\exp(\mathrm{i}\varphi_1) + E_{02}\exp(\mathrm{i}\varphi_2)][E_{01}\exp(-\mathrm{i}\varphi_1) + E_{02}\exp(-\mathrm{i}\varphi_2)] \\ &= E_{01}^2 + E_{02}^2 + 2E_{01}E_{02}[\cos(\varphi_2 - \varphi_1)] \\ &= I_1 + I_2 + 2\sqrt{I_1 I_2}[\cos(\varphi_2 - \varphi_1)],\end{aligned} \tag{S11}$$

where I_1 and I_2 are the position-independent intensities of the two separate electric fields, such that $I_1 = \bar{E}_1\bar{E}_1^* = |\bar{E}_1|^2 = E_{01}^2$ and $I_2 = \bar{E}_2\bar{E}_2^* = |\bar{E}_2|^2 = E_{02}^2$, while $2\sqrt{I_1 I_2}[\cos(\varphi_2 - \varphi_1)]$ is the position-dependent interference term. Here $(\varphi_2 - \varphi_1)$ is the phase difference between the two electromagnetic plane waves at a given position $\mathbf{r}$ in 3D space.

Equation (S11) describes the three-dimensional intensity profile (interference pattern) that we can observe when two coherent beams of electromagnetic radiation intersect each other – although this description is only strictly valid for beams that are infinitely wide. Here, the beams are approximated by plane waves and their coherence poses the constraint $|\boldsymbol{k_1}| = |\boldsymbol{k_2}| = k_\lambda = 2\pi n_\lambda/\lambda$. Notably, this constraint also justifies our initial omission of the time-dependent term in our definition of the complex electric field of an electromagnetic plane wave [Eq. (S1) and Eq. (S2)], as this time-dependent term would be absent from Eq. (S11) if the two electromagnetic plane waves are coherent.

2.3 Description of the subset of interference patterns relevant for the YPFM microscope

We now focus on characterizing the subset of interference patterns described by Eq. (S11) that oscillate only in directions parallel to the xy-plane. Using Eq. (S3) we define the angular wave vectors $\mathbf{k_1}$ and $\mathbf{k_2}$ of the two coherent electromagnetic plane waves introduced in Eqs. (S6-9),

$$\mathbf{k_1} = k_\lambda \sin\theta_1 \cos\beta_1\, \mathbf{e}_\mathrm{x} + k_\lambda \sin\theta_1 \sin\beta_1\, \mathbf{e}_\mathrm{y} + k_\lambda \cos\theta_1\, \mathbf{e}_\mathrm{z}, \tag{S12}$$

$$\mathbf{k_2} = k_\lambda \sin\theta_2 \cos\beta_2\, \mathbf{e}_\mathrm{x} + k_\lambda \sin\theta_2 \sin\beta_2\, \mathbf{e}_\mathrm{y} + k_\lambda \cos\theta_2\, \mathbf{e}_\mathrm{z}. \tag{S13}$$

Next, we find the phase difference $\varphi_2 - \varphi_1$ in Eq. (S11) by combining Eq. (S4), Eqs. (S8), Eq. (S9), Eq. (S12), and Eq. (S13),

$$\begin{aligned}\varphi_2 - \varphi_1 = \;& (\mathbf{k_2}\cdot\mathbf{r} + \varphi_{02}) - (\mathbf{k_1}\cdot\mathbf{r} + \varphi_{01}) \\ = \;& xk_\lambda(\sin\theta_2\cos\beta_2 - \sin\theta_1\cos\beta_1) \\ &+ yk_\lambda(\sin\theta_2\sin\beta_2 - \sin\theta_1\sin\beta_1) \\ &+ zk_\lambda(\cos\theta_2 - \cos\theta_1) + (\varphi_{02} - \varphi_{01}).\end{aligned} \tag{S14}$$

Examining the cosine function in Eq. (S11), we observe that constructive interference occurs when the phase difference $\varphi_2 - \varphi_1$ described in Eq. (S14) satisfies the equation

$$\varphi_2 - \varphi_1 = 2\pi m\,, \tag{S15}$$

where $m = 0, \pm1, \pm2, \cdots$.

By combining Eq. (S14) and Eq. (S15), we see that constructive interference occurs at coordinates (x, y, z) satisfying the equation

$$\begin{aligned}[2\pi m - (\varphi_{02} - \varphi_{01})]/k_\lambda = \quad & x(\sin\theta_2 \cos\beta_2 - \sin\theta_1 \cos\beta_1) \\ + \; & y(\sin\theta_2 \sin\beta_2 - \sin\theta_1 \sin\beta_1) \\ + \; & z(\cos\theta_2 - \cos\theta_1). \end{aligned} \tag{S16}$$

For nearly all choices of θ_1, θ_2, β_1, β_2, φ_{01}, φ_{02}, (i.e., nearly all definitions of $\mathbf{k_1}$ and $\mathbf{k_2}$) valid combinations of x, y and z in Eq. (S16) will trace parallel and equally spaced planes in 3D space, marking the ridges of the constructive interference planes in the spatially oscillating interference pattern described by Eq. (S11). Exceptions are when θ_1, θ_2, β_1, and β_2, are chosen such that the two electromagnetic plane waves propagate in the same direction, i.e., when $\mathbf{k_1} = \mathbf{k_2}$. That is, when $\theta_1 = \theta_2 = 0$, when $\theta_1 = \theta_2 = \pi$, or when $\theta_1 = \theta_2$ while $\beta_1 = \beta_2$.

We now describe the spatial period of the interference pattern along the x-axis and y-axis. By equating y and z to zero in Eq. (S16) we obtain

$$x = \frac{2\pi m - (\varphi_{02} - \varphi_{01})}{k_\lambda(\sin\theta_2 \cos\beta_2 - \sin\theta_1 \cos\beta_1)}. \tag{S17}$$

So, we can express the spatial period Δx of the interference pattern along the x-axis by subtracting the x-coordinates of adjacent constructive interference planes defined by $m = 0$ and $m = 1$, respectively,

$$\Delta x = x(m = 1) - x(m = 0). \tag{S18}$$

Upon substitution from Eq. (S17), this reduces to

$$\Delta x = \frac{2\pi}{k_\lambda(\sin\theta_2 \cos\beta_2 - \sin\theta_1 \cos\beta_1)}. \tag{S19}$$

Similarly, by equating x and z to zero in Eq. (S16) we can express the spatial period Δy of the interference pattern along the y-axis

$$\Delta y = \frac{2\pi}{k_\lambda(\sin\theta_2 \sin\beta_2 - \sin\theta_1 \sin\beta_1)}. \tag{S20}$$

To describe the spatial period of the subset of interference patterns that oscillate only in the xy-plane (i.e., no oscillations along the z-axis), we introduce two additional constraints ensuring that $\mathbf{k_1}$ and $\mathbf{k_2}$ are geometric reflections through the z-axis, namely: $\theta_1 = \theta_2 = \theta$ and $\beta_1 + \pi = \beta_2 = \beta$, which, when inserted into Eq. (S19) and Eq. (S20), yields

$$\Delta x = \frac{\pi}{k_\lambda \sin\theta \cos\beta}, \tag{S21}$$

$$\Delta y = \frac{\pi}{k_\lambda \sin\theta \sin\beta}. \tag{S22}$$

2.4 Description of the relevant subset of interference patterns relative to the field of view and the numerical aperture of the imaging objective in the YPFM microscope

We consider a square field of view (FOV) spanning the interval $[-L/2, L/2] \times [-L/2, L/2]$ in the xy-plane, where L is the side-length of the FOV. For an interference pattern imprinted across this FOV, we can describe the number of oscillations n_x along the x-axis and within the FOV by $n_x = L/\Delta x$ and, similarly, $n_y = L/\Delta y$. By combining these definitions with Eq. (S21) and Eq. (S22), we obtain

$$n_x = \frac{L k_\lambda \sin\theta \cos\beta}{\pi}, \tag{S23}$$

$$n_y = \frac{L k_\lambda \sin\theta \sin\beta}{\pi}. \tag{S24}$$

In the YPFM microscope presented here, we project two coherent electromagnetic beams of light through an imaging objective and onto a fluorophore-labeled sample located within the FOV. In the 3D space around the sample spanned by $\mathbf{e}_x$, $\mathbf{e}_y$, and $\mathbf{e}_z$, we describe these two beams as plane waves with the angular wave vectors $\mathbf{k_1}$ and $\mathbf{k_2}$ defined in Eq. (S12) and Eq. (S13). We inject the two beams into the imaging objective at two positions that reflect each other geometrically through the center-coordinate ($n_x = n_y = 0$) of the pupil plane, thus satisfying $n_{x1} = -n_{x2} = n_x$ and $n_{y1} = -n_{y2} = n_y$, where the subscripts (1 and 2) identify the individual beams (as in $\mathbf{k_1}$ and $\mathbf{k_2}$). This ensures that the two beams satisfy the constraints $\theta_1 = \theta_2 = \theta$ and $\beta_1 + \pi = \beta_2 = \beta$, thus forming interference patterns that oscillate only along the x and y-axes as derived above. The numbers of oscillations (n_x and n_y) across the 2D FOV in these interference patterns are described by Eq. (S23) and Eq. (S24).

The numerical aperture (NA) of the imaging objective, given by $\mathrm{NA} = n_\lambda \sin\theta_{\max}$ (where n_λ is the refractive index of the immersion medium, aka. propagation medium), confines the polar angle (θ) of the beams to the interval $[0 \le \theta \le \theta_{\max}]$. By substituting this constraint into Eq. (S23) and Eq. (S24), we can express how the imaging objective constrains the number of oscillations (n_x and n_y) we can imprint across the FOV,

$$n_x \le \frac{L k_\lambda \,\mathrm{NA} \cos\beta}{n_\lambda \pi}, \tag{S25}$$

$$n_y \le \frac{L k_\lambda \,\mathrm{NA} \sin\beta}{n_\lambda \pi}. \tag{S26}$$

If Eq. (S25) and Eq. (S26) are not satisfied, then the beams will be rejected by the circular back-aperture in the pupil plane of the objective. We caution that n_x and n_y should not be confused with the refractive index of the immersion/propagation medium (n_λ).

2.5 Definition of the probe patterns used in the YPFM microscope

As detailed above, the YPFM microscope presented here satisfies the constraints $\theta_1 = \theta_2 = \theta$ and $\beta_1 + \pi = \beta_2 = \beta$. By inserting these constraints into Eq. (S14), we can describe the phase difference ($\varphi_2 - \varphi_1$) of the two plane waves that form the interference pattern as

$$\varphi_2 - \varphi_1 = 2x k_\lambda \sin\theta \cos\beta + 2y k_\lambda \sin\theta \sin\beta + (\varphi_{02} - \varphi_{01}). \tag{S27}$$

By combining Eq. (S23) and Eq. (S24) with Eq. (S27), we can also express this phase difference $\varphi_2 - \varphi_1$ as

$$\varphi_2 - \varphi_1 = x\frac{2\pi n_x}{L} + y\frac{2\pi n_y}{L} + (\varphi_{02} - \varphi_{01}). \tag{S28}$$

Here, we note that Eq. (S28) describes a phase difference between two plane waves, and this phase difference corresponds to the phase [cosine term in Eq. (S11)] of the subset of interference patterns used in the YPFM microscope presented here.

We also note that, in practice, the interfering beams are not plane waves. Thus, we describe the shape of the interference pattern as the plane-wave interference pattern (treated above) modulated by a quasi-Gaussian envelope function, $g(x, y)$, which, at low NA and within a reasonable distance from the point where the two beams intersect (i.e., $x = y = z = 0$), may be modelled as independent of spatial frequencies (k_x, k_y, k_z) and z-position. By introducing this dimensionless envelope function $g(x, y)$ in Eq. (S11) (i.e., multiplying it onto the right-hand side of the equation), substituting Eq. (S28) into Eq. (S11), and then equating the intensities of the two plane waves such that $I_1 = I_2 = ½I_0$, we can express the intensity distribution $I(x, y)$ of the interference patterns used in the YPFM microscope as

$$I(x, y) = I_0\, g(x, y)\, \left\{1 + \cos\left[x\frac{2\pi n_x}{L} + y\frac{2\pi n_y}{L} + (\varphi_{02} - \varphi_{01})\right]\right\}. \tag{S29}$$

Notice that the interference pattern $I(x, y)$ exists in three-dimensional space, but it is independent of z-position.

When n_x and n_y are integers [satisfying Eq. (S25) and Eq. (S26)], we call these intensity distributions probe patterns and write them in the more convenient form

$$I(x, y) = I_0\, g(x, y)\, \{1 + \cos[x k_x(n_x) + y k_y(n_y) + \phi]\}, \tag{S30}$$

with

$$k_x(n_x) = \frac{2\pi n_x}{L}, \tag{S31}$$

$$k_y(n_y) = \frac{2\pi n_y}{L}, \tag{S32}$$

$$\phi = \varphi_{02} - \varphi_{01}. \tag{S33}$$

Here ϕ is the phase offset of the probe pattern in units of [rad], and $k_x(n_x)$ and $k_y(n_y)$ are spatial frequencies of the probe pattern in units of [rad m^{-1}] with integer (and dimensionless) numbers of oscillations (n_x and n_y) across the FOV along the x-axis and y-axis, respectively. We caution that k_x and k_y should not be confused with the angular wave number (k_λ).

In summary, Eq. (S30) represents a convenient description of the probe patterns used in the YPFM microscope presented here. This equation ignores effects of polarization (which is inadequate at high NA). This equation also approximates the envelope function as independent of spatial frequencies (k_x, k_y, k_z) and z-position (which may also be inadequate at high NA). The probe patterns span a square FOV $[-L/2, L/2] \times [-L/2, L/2]$ with the side length L. The probe patterns are formed through interference of two coherent beams of radiation with equal intensities. These beams are geometric reflections of each other through the z-axis (the optical axis of the imaging objective) but their separate initial phases (φ_{01} and φ_{02}) are independent.

The 3D Cartesian coordinates (x, y, z) may be visualized as a spatial domain, where (x, y, z) represent physical positions in the space around the sample. The 2D Cartesian coordinates (k_x, k_y) represent (part of) the corresponding frequency domain, where (k_x, k_y) are coordinates directly (at least at low NA) proportional to the physical coordinates in the pupil plane of the imaging objective where the two beams are injected to form a given probe pattern across the FOV. Next, we will expound how these definitions of the spatial domain and the frequency domain are conveniently linked via the discrete Fourier transform.

Supplementary Note 3
Mathematical description of image formation in YPFM imaging

3.1 Definition of the sum-projection (z-axis integral) image obtained with the YPFM microscope by using the discrete Fourier transform

In the YPFM microscope, we consider a sample positioned in a square FOV, with side length L, spanning the 2D interval $[-L/2, L/2] \times [-L/2, L/2]$ in the xy-plane. Here, in the spatial domain, we describe the 3D spatial distribution of entities that provide contrast (e.g., the 3D spatial distribution of fluorophores) by the function $f(x, y, z)$. We also introduce the integral $f_{\downarrow z}(x, y)$ of the function $f(x, y, z)$ along the z-axis (denoted the 'sum-projection' or $\downarrow z$),

$$f_{\downarrow z}(x, y) = \int_{-\infty}^{\infty} f(x, y, z)\, \mathrm{d}z. \tag{S34}$$

In the YPFM microscope presented here, it is exactly the sum-projection $f_{\downarrow z}(x, y)$ multiplied by the z-independent, quasi-Gaussian envelope function, $g(x, y)$ that we image. Thus, we define the two-dimensional function $\Omega_{\downarrow z}(x, y)$ such that

$$\Omega_{\downarrow z}(x, y) = f_{\downarrow z}(x, y)\; g(x, y). \tag{S35}$$

Using a truncated Fourier series, i.e., a partial sum, rather than the infinite sum from the complete Fourier series (Kreyszig *et al.*[9], p. 528), we can approximate the ideal image $\Omega_{\downarrow z}(x, y)$ by

$$\widetilde{\Omega}_{\downarrow z}^{N}(x, y) = \sum_{n_x=-N}^{N} \sum_{n_y=-N}^{N} \hat{c}\left(n_x, n_y\right)\, e^{i\left[k_x(n_x)\mathrm{x} + k_y(n_y)y\right]}, \tag{S36}$$

with

$$\hat{c}\left(n_x, n_y\right) = \frac{1}{L^2} \int_{-L/2}^{L/2} \int_{-L/2}^{L/2} f_{\downarrow z}(x, y)\; g(x, y)\; e^{-i\left[k_x(n_x)\mathrm{x} + k_y(n_y)y\right]}\, \mathrm{d}y\, \mathrm{d}x. \tag{S37}$$

That is, $\widetilde{\Omega}_{\downarrow z}^{N}(x, y)$ is a weighted sum of a finite set of 2D Fourier basis functions, i.e., complex 2D sinusoids that do not vary along the z-axis. The complex Fourier coefficient $\hat{c}\left(n_x, n_y\right)$ describes the weight of a complex 2D sinusoid with n_x and n_y oscillations across intervals of length $L_x = L$ and $L_y = L$ along the x-axis and y-axis, respectively, with $k_x(n_x) = 2\pi n_x L_x^{-1}$ and $k_y\left(n_y\right) = 2\pi n_y L_y^{-1}$. In this truncated Fourier series, n_x and n_y are integers in the intervals $n_x \in [-N_x, N_x]$ and $n_y \in \left[-N_y, N_y\right]$, while $N_x = N$ and $N_y = N$ are positive integers representing the maximum numbers of spatial oscillations (along the x-axis and y-axis, respectively) represented in the approximation $\widetilde{\Omega}_{\downarrow z}^{N}(x, y)$ to the underlying function $\Omega_{\downarrow z}(x, y)$. It follows that $\widetilde{\Omega}_{\downarrow z}^{N}(x, y)$ will approximate $\Omega_{\downarrow z}(x, y)$ better for larger values of N. We emphasize that $\Omega_{\downarrow z}(x, y)$ is a real-valued function. So, assuming ideal imaging conditions, Eq. (S37) satisfies

$$\hat{c}\left(n_x, n_y\right) = \hat{c}\left(-n_x, -n_y\right)^{*}, \tag{S38}$$

where * denotes complex conjugation. It follows that $\widetilde{\Omega}_{\downarrow z}^{N}(x, y)$ is also a real-valued function.

We only use the complex Fourier series, because the real-valued basis functions of a 2D Fourier transform are mathematically unwieldy[9].

3.2 Description of signal readouts in the YPFM microscope

To capture an image with the YPFM microscope, we record a series of signals S proportional to, e.g., the fluorescence intensity from a single-element detector. The signal S varies as different probe patterns $I(x, y, n_x, n_y, \phi)$ as described by Eq. (S30) are imprinted across, e.g., a 3D spatial distribution of fluorophores $f(x, y, z)$.

If we assume a direct proportionality between the actual signal and the measured signal S and also ignore physical scale factors as, e.g., detector gain, we can express the measured signal as the 3D integral of the product between f and I,

$$S(n_x, n_y, \phi) = \int_{-L/2}^{L/2}\int_{-L/2}^{L/2}\int_{-\infty}^{\infty} f(x, y, z)\, I(x, y, n_x, n_y, \phi)\, \mathrm{d}z\, \mathrm{d}y\, \mathrm{d}x\,. \tag{S39}$$

As I is independent of z, a combination of Eq. (S34) with Eq. (S39) yields

$$S(n_x, n_y, \phi) = \int_{-L/2}^{L/2}\int_{-L/2}^{L/2} f_{\downarrow z}(x, y)\, I(x, y, n_x, n_y, \phi)\, \mathrm{d}y\, \mathrm{d}x, \tag{S40}$$

where S is non-negative and real-valued.

3.3 Computation of Fourier coefficients from discrete signal readouts

In accord with previous work by Zhang *et al.*[10], we imprint four probe patterns with $\pi/2$ rad intervals and use the resulting signal readouts to cancel out signal contributions from non-oscillating terms in the probe pattern, i.e., the n_x and n_y-independent terms in Eq. (S30). Specifically, we imprint probe patterns with $\phi = [0,\ \pi/2\,,\ \pi,\ 3\pi/2]$ rad for each set of spatial frequencies. To express these four probe patterns in a compact form, we insert $\phi = [0,\ \pi/2\,,\ \pi,\ 3\pi/2]$ rad in Eq. (S30) and use the trigonometric identities $[\cos(\xi \pm \pi/2) = \sin(\mp\xi)]$, yielding

$$I(x, y, n_x, n_y, \phi = 0) = I_0\, g(x, y)\, \{1 + \cos[xk_x(n_x) + yk_y(n_y)]\}, \tag{S41}$$

$$I(x, y, n_x, n_y, \phi = \pi/2) = I_0\, g(x, y)\, \{1 - \sin[xk_x(n_x) + yk_y(n_y)]\}, \tag{S42}$$

$$I(x, y, n_x, n_y, \phi = \pi) = I_0\, g(x, y)\, \{1 - \cos[xk_x(n_x) + yk_y(n_y)]\}, \tag{S43}$$

$$I(x, y, n_x, n_y, \phi = 3\pi/2) = I_0\, g(x, y)\, \{1 + \sin[xk_x(n_x) + yk_y(n_y)]\}. \tag{S44}$$

By inserting Eqs. (S41-S44) into Eq. (S40), we can express the signals measured by the single-element detector as

$$S(n_x, n_y, \phi = 0) = I_0 \int_{-L/2}^{L/2}\int_{-L/2}^{L/2} f_{\downarrow z}(x, y)\, g(x, y)\, \{1 + \cos[xk_x(n_x) + yk_y(n_y)]\}\, \mathrm{d}y\, \mathrm{d}x, \tag{S45}$$

$$S(n_x, n_y, \phi = \pi/2) = I_0 \int_{-L/2}^{L/2}\int_{-L/2}^{L/2} f_{\downarrow z}(x, y)\, g(x, y)\, \{1 - \sin[xk_x(n_x) + yk_y(n_y)]\}\, \mathrm{d}y\, \mathrm{d}x, \tag{S46}$$

$$S(n_x, n_y, \phi = \pi) = I_0 \int_{-L/2}^{L/2}\int_{-L/2}^{L/2} f_{\downarrow z}(x, y)\, g(x, y)\, \{1 - \cos[xk_x(n_x) + yk_y(n_y)]\}\, \mathrm{d}y\, \mathrm{d}x, \tag{S47}$$

$$S(n_x, n_y, \phi = 3\pi/2) = I_0 \int_{-L/2}^{L/2}\int_{-L/2}^{L/2} f_{\downarrow z}(x, y)\, g(x, y)\, \{1 + \sin[xk_x(n_x) + yk_y(n_y)]\}\, \mathrm{d}y\, \mathrm{d}x. \tag{S48}$$

Now, we want to express the complex coefficient $\hat{c}(n_x, n_y)$ in Eq. (S37) as a function of signals S measured by the single-element detector. First, we describe the differences between pairs of signals S measured with probe patterns of π rad phase-difference. Specifically, we find $S(n_x, n_y, 0) - S(n_x, n_y, \pi)$ by subtracting Eq. (S47) from Eq. (S45), and then substituting from Eq. (S41) and Eq. (S43). This gives

$$S(n_x, n_y, 0) - S(n_x, n_y, \pi) = 2I_0 \int_{-L/2}^{L/2} \int_{-L/2}^{L/2} f_{\downarrow z}(x, y)\, g(x, y) \cos\left[x k_x(n_x) + y k_y(n_y)\right] \mathrm{d}y\, \mathrm{d}x. \quad \text{(S49)}$$

Then we find $S(n_x, n_y, \pi/2) - S(n_x, n_y, 3\pi/2)$ by subtracting Eq. (S48) from Eq. (S46), and then substituting from Eq. (S42) and Eq. (S44). The result is

$$S(n_x, n_y, \pi/2) - S(n_x, n_y, 3\pi/2) = -2I_0 \int_{-L/2}^{L/2} \int_{-L/2}^{L/2} f_{\downarrow z}(x, y)\, g(x, y) \sin\left[x k_x(n_x) + y k_y(n_y)\right] \mathrm{d}y\, \mathrm{d}x. \quad \text{(S50)}$$

Next, we express the quantity $\left[S(n_x, n_y, 0) - S(n_x, n_y, \pi)\right] + i\left[S(n_x, n_y, \pi/2) - S(n_x, n_y, 3\pi/2)\right]$, by multiplying Eq. (S50) by the imaginary unit and then adding the resulting equation to Eq. (S49). This becomes

$$\begin{aligned} &\left[S(n_x, n_y, 0) - S(n_x, n_y, \pi)\right] + i\left[S(n_x, n_y, \pi/2) - S(n_x, n_y, 3\pi/2)\right] \\ &= 2I_0 \int_{-L/2}^{L/2} \int_{-L/2}^{L/2} f_{\downarrow z}(x, y)\, g(x, y) \left\{\cos\left[x k_x(n_x) + y k_y(n_y)\right] - i \sin\left[x k_x(n_x) + y k_y(n_y)\right]\right\} \mathrm{d}y\, \mathrm{d}x. \quad \text{(S51)} \end{aligned}$$

Using Euler's formula $e^{-i\xi} = \cos(\xi) - i\sin(\xi)$ and dividing by $2I_0$, Eq. (S51) reduces to

$$\begin{aligned} &\frac{1}{2I_0}\left\{\left[S(n_x, n_y, 0) - S(n_x, n_y, \pi)\right] + i\left[S(n_x, n_y, \pi/2) - S(n_x, n_y, 3\pi/2)\right]\right\} \\ &= \int_{-L/2}^{L/2} \int_{-L/2}^{L/2} f_{\downarrow z}(x, y) g(x, y) \mathrm{e}^{-i\left[x k_x(n_x) + y k_y(n_y)\right]} \mathrm{d}y\, \mathrm{d}x. \end{aligned} \quad \text{(S52)}$$

As the double integrals in Eq. (S37) and Eq. (S52) are identical, we can now express $\hat{c}(n_x, n_y)$ as a function of S, simply by substituting the lefthand side of Eq. (S52) into Eq. (S37)

$$\hat{c}(n_x, n_y) = \frac{1}{2I_0 L^2}\left\{\left[S(n_x, n_y, 0) - S(n_x, n_y, \pi)\right] + i\left[S(n_x, n_y, \pi/2) - S(n_x, n_y, 3\pi/2)\right]\right\}. \quad \text{(S53)}$$

In summary, we can use Eq. (S36) to form an image, $\widetilde{\Omega}_{\downarrow z}^{N}(x, y)$, of a sample by sequentially imprinting well-defined probe patterns onto the sample, while recording the resulting accumulated signals S using a single-element detector. Specifically, we must imprint probe patterns for measuring S, such that we can compute $\hat{c}(n_x, n_y)$ in Eq. (S53) for all combinations of $n_x \in [-N_x, N_x]$ and $n_y \in [-N_y, N_y]$, while $N_x = N_y = N$ represents a user-defined, square spatial frequency confine.

The spatial frequency confine represents the range of spatial frequencies that are reproduced in the image. As such, the spatial frequency confine is closely related to the optical transfer function (OTF) of the imaging system. Since our probe patterns do not vary along the z-axis ($k_z = 0$), all spatial frequencies reproduced in the image lie within the (k_x, k_y)-plane. In other words, the OTF is a flat 2D plane in 3D Fourier space.

Notice that because for our case $\Omega_{\downarrow z}(x,y)$ is a real-valued function, Eq. (S38) is valid and the Fourier coefficients are geometrically symmetric complex conjugates about the origin of the (n_x, n_y)-coordinate system. This symmetry may be exploited to reduce image acquisition time.

3.4 Evaluation of the discrete Fourier transform using the fast Fourier transform

An YPFM image, is a discrete sampling of the continuous function $\widetilde{\Omega}^N_{\downarrow z}(x,y)$ across positions $(x(m_x), y(m_y))$ arranged equidistantly (by $\Delta = L/M$) in a square lattice, representing the FOV, with an arbitrary number, $M \geq 2N+1$, of positions (pixels) along each side of the lattice, such that

$$x(m_x) = -\frac{L}{2} + \Delta\left(\frac{1}{2} + m_x\right) \quad \text{for} \quad m_x = 0,1,2 \dots M-1, \tag{S54}$$

and

$$y(m_y) = -\frac{L}{2} + \Delta\left(\frac{1}{2} + m_y\right) \quad \text{for} \quad m_y = 0,1,2 \dots M-1. \tag{S55}$$

Using these definitions, and by substituting from Eq. (S31) and Eq. (S32), we can rewrite Eq. (S36) to express the discrete YPFM image.

$$\widetilde{\Omega}^N_{\downarrow z}(m_x, m_y) = \sum_{n_x=-N}^{N} \sum_{n_y=-N}^{N} \hat{c}(n_x, n_y)\, e^{-i\pi(n_x+n_y)}\, e^{\frac{i\pi(n_x+n_y)}{M}}\, e^{\frac{i2\pi(n_x m_x + n_y m_y)}{M}} \tag{S56}$$

Now, we can form a YPFM image by evaluating Eq. (S56). There are, however, still two important caveats to consider:

First, it is advantageous to compute $\left|\widetilde{\Omega}^N_{\downarrow z}(m_x, m_y)\right|$ rather than $\widetilde{\Omega}^N_{\downarrow z}(m_x, m_y)$, where '$|\ \ |$' denotes the absolute value. This is because the absolute value circumvents drawbacks related to long-term phase drift, as detailed in **Supplementary Note 6**. Indeed, all YPFM images displayed here are computed as $\left|\widetilde{\Omega}^N_{\downarrow z}(m_x, m_y)\right|$.

Second, the computational cost of evaluating Eq. (S56) increases quadratically, as the spatial frequency confine N increases. For practical values of N, e.g., $N = 35$, the computational cost is prohibitive, even with a good PC. We can alleviate this issue by using the fast Fourier transform (FFT), i.e., a computationally efficient implementation of the discrete Fourier transform. However, this is not completely straightforward, because our Fourier coefficients, $\hat{c}(n_x, n_y)$, are organized in a symmetric series with $n_x \in [-N_x, N_x]$ and $n_y \in [-N_y, N_y]$, which is not immediately compatible with the ordinary 2DFFT functions. To circumvent this problem, it is advantageous to partition the 2D Fourier sum in Eq. (S56) into the zero-frequency coefficient $[\hat{c}(0,0)]$ and eight FFT-compatible constituents: four 1D Fourier sums [across $\hat{c}(n_x, 0)$ and $\hat{c}(0, n_y)$, for negative and positive n_x and n_y], and four 2D Fourier sums [across $\hat{c}(n_x, n_y)$ for negative and positive n_x and n_y]. This partitioning manifests as a sizeable expansion of the right-hand side of Eq. (S56).

$$
\begin{aligned}
\widetilde{\Omega}_{\downarrow z}^{N}(m_x, m_y) = \quad & \hat{c}(0,0) \\
& + \sum_{n_x=1}^{N} \hat{c}(n_x, 0)\, e^{-i\pi n_x}\, e^{\frac{i\pi n_x}{M}}\, e^{\frac{i2\pi n_x m_x}{M}} \\
& + \sum_{n_x=1}^{N} \hat{c}(-n_x, 0)\, e^{i\pi n_x}\, e^{-\frac{i\pi n_x}{M}}\, e^{-\frac{i2\pi n_x m_x}{M}} \\
& + \sum_{n_y=1}^{N} \hat{c}(0, n_y)\, e^{-i\pi n_y}\, e^{\frac{i\pi n_y}{M}}\, e^{\frac{i2\pi n_y m_y}{M}} \\
& + \sum_{n_y=1}^{N} \hat{c}(0, -n_y)\, e^{i\pi n_y}\, e^{-\frac{i\pi n_y}{M}}\, e^{-\frac{i2\pi n_y m_y}{M}} \\
& + \sum_{n_x=1}^{N} \sum_{n_y=1}^{N} \hat{c}(n_x, n_y)\, e^{-i\pi(n_x+n_y)}\, e^{\frac{i\pi(n_x+n_y)}{M}}\, e^{\frac{i2\pi(n_x m_x+n_y m_y)}{M}} \\
& + \sum_{n_x=1}^{N} \sum_{n_y=1}^{N} \hat{c}(-n_x, n_y) e^{i\pi(n_x-n_y)}\, e^{-\frac{i\pi(n_x-n_y)}{M}}\, e^{-\frac{i2\pi(n_x m_x-n_y m_y)}{M}} \\
& + \sum_{n_x=1}^{N} \sum_{n_y=1}^{N} \hat{c}(n_x, -n_y)\, e^{-i\pi(n_x-n_y)}\, e^{\frac{i\pi(n_x-n_y)}{M}}\, e^{\frac{i2\pi(n_x m_x-n_y m_y)}{M}} \\
& + \sum_{n_x=1}^{N} \sum_{n_y=1}^{N} \hat{c}(-n_x, -n_y)\, e^{i\pi(n_x+n_y)}\, e^{-\frac{i\pi(n_x+n_y)}{M}}\, e^{-\frac{i2\pi(n_x m_x+n_y m_y)}{M}}
\end{aligned} \tag{S57}
$$

The twelve sums in Eq. (S57) can be evaluated using six 1DFFTs and six inverse equivalents (1DiFFTs) as detailed below (Press *et al.*[11], p. 515). To satisfy the input format of the FFT function, the sums are computed by inputting vectors of M elements and 2D matrices of M-by-M elements, where vector/matrix elements not included in the sum are set to zero. If we let M exceed $2N + 1$, we are effectively zero padding the Fourier sum in Eq. (S56). This results in an image with more (and smaller) pixels across the FOV, but it does not add information in terms of image resolution.

If we use a zero-based indexing scheme $[0,1,2 \ldots M-1]$, the product of our Fourier coefficients and corresponding phase-shifting coefficients, i.e., all except the rightmost exponential in each of the sums in Eq. (S57), will be indexed by $[1 \ldots N]$ in vectors and by $[1 \ldots N, 1 \ldots N]$ in 2D matrices, prior to applying the 1DFFT and 1DiFFT functions. We exemplify below.

Example (first sum): We can evaluate the first sum in Eq. (S57) by using a 1DFFT function (not 1DiFFT) as the index n_x is positive in $\hat{c}(n_x, 0)$. Specifically, we feed the M-by-1 vector

$$
\boldsymbol{q_1}(m_x, 0) = \begin{cases} \hat{c}(m_x, 0)\, e^{-i\pi m_x}\, e^{\frac{i\pi m_x}{M}} & \text{for } m_x = 1 \ldots N \\ 0 & \text{for } m_x = 0 \text{ and } N+1 \le m_x \le M-1, \end{cases} \tag{S58}
$$

into the 1DFFT function, yielding another M-by-1 vector. Finally, we replicate this resulting vector M times across the y-dimension, yielding a M-by-M matrix which represents the image contribution from the first sum.

Example (fourth sum): We can evaluate the fourth sum in Eq. (S57) by using a 1DiFFT function (not 1DFFT) as the index n_y is negative in $\hat{c}(0, -\mathrm{n_y})$. Specifically, we feed the 1-by-M vector

$$\boldsymbol{q_4}(0, m_y) = \begin{cases} \hat{c}(0, -m_y)\, e^{i\pi m_y}\, e^{-\frac{i\pi m_y}{M}} & \text{for } m_y = 1 \dots N \\ 0 & \text{for } m_y = 0 \text{ and } N+1 \le m_y \le M-1 \end{cases} \tag{S59}$$

into the 1DiFFT function, yielding another 1-by-M vector. Finally, we replicate this resulting vector M times across the x-dimension, yielding a M-by-M matrix which represents the image contribution from the fourth sum.

Example (second double sum): Following the same logic as in the two previous examples, we can evaluate the double sum across $\hat{c}(-n_x, n_y)$ in Eq. (S57) by using a 1DiFFT function (across the x-dimension) and a 1DFFT function (across the y-dimension). Specifically, we feed the M-by-M matrix

$$\boldsymbol{Q_2}(m_x, m_y) = \begin{cases} \hat{c}(-m_x, m_y) e^{i\pi(m_x - m_y)}\, e^{-\frac{i\pi(m_x - m_y)}{M}} & \text{for } m_x = 1 \dots N\,, m_y = 1 \dots N \\ 0 & \text{for } m_x = 0 \text{ and } N+1 \le m_x \le M-1 \\ 0 & \text{for } m_y = 0 \text{ and } N+1 \le m_y \le M-1, \end{cases} \tag{S60}$$

into the 1DiFFT function (applied along the x-dimension), yielding another M-by-M matrix, which we feed into the 1DFFT function (applied along the y-dimension). The resulting M-by-M matrix represents the image contribution from the second double sum.

Supplementary Note 4
Spatial resolution in YPFM imaging

4.1 Expected spatial resolution in the YPFM microscope

Using Eq. (S57) we can model how a given contrast distribution $f(x, y, z)$ will manifest in an YPFM image. This allows us to evaluate imaging resolution as a function of the user-defined spatial frequency confine N, assuming ideal conditions, i.e., noise/aberration-free, and perfect system calibration. In our numerical simulations, we measured imaging resolution as the full width at half maximum (FWHM) of a 2D Gaussian function fitted to simulated images representing an infinitely small emitter (a point emitter). Thus, we found the approximate relationship

$$\mathrm{FWHM}_{\mathrm{YPFM,sim}} \approx 1.1\frac{L}{2N} \tag{S61}$$

which is very close to

$$\mathrm{FWHM}_{\mathrm{Nyquist}} = \frac{L}{2N}, \tag{S62}$$

where $L/2N$ is half of the wavelength of the probe pattern with highest spatial frequency as measured along the x- or y-axis. The subscript 'Nyquist' was chosen to reflect our own paraphrasing of the Nyquist-Shannon theorem: "*When two infinitely small points (e.g., emitters) are represented in an image, we can only hope to resolve them, if they are separated by a distance, which equals or exceeds half the wavelength of the shortest wave constituent (highest spatial frequency) recapitulated in said image*". In this paraphrasing, we emphasize '*hope to*', as an unbalanced representation of spatial frequencies (within the spatial frequency confine) will result in artifacts, notably blurring if low spatial frequencies are overrepresented as is the case in widefield microscopy.

4.2 Expected spatial resolution in a NA-equivalent widefield microscope

To best compare resolution measures in our YPFM microscope against established resolution measures in widefield microscopy, we must describe an NA-equivalent to the spatial frequency confine N. First, we combine Eq. (S25) and Eq. (S26) to describe combinations of n_x and n_y that fall within the circular spatial frequency support of the imaging objective. To condense this expression, we substitute $k_\lambda = 2\pi n_\lambda/\lambda$ and get

$$\sqrt{n_x^2 + n_y^2} \leq \sqrt{\left(\frac{Lk_\lambda\ \mathrm{NA}\cos\beta}{n_\lambda\pi}\right)^2 + \left(\frac{Lk_\lambda\ \mathrm{NA}\sin\beta}{n_\lambda\pi}\right)^2} = \frac{2L\ \mathrm{NA}}{\lambda} \tag{S63}$$

We note that if Eq. (S63) is not satisfied, the two beams used in our YPFM microscope will be rejected by the circular back-aperture of the imaging objective. We also note that it is not straightforward to 'translate' the spatial frequency confine, which is square in (n_x,n_y)-coordinates, to an NA-equivalent, which would describe a circular frequency support. Thus, we isolate NA in Eq. (S63) and describe the NA-equivalent ($\mathrm{NA_{eq}}$) at two extremes:

$$\mathrm{NA}_{\mathrm{eq,min}} = \frac{\lambda N}{2L}, \tag{S64}$$

where $n_x = N$ and $n_y = 0$, thus inscribing the circular spatial frequency support in the square spatial frequency confine, and

$$\mathrm{NA}_{\mathrm{eq,max}} = \frac{\sqrt{2}\,\lambda N}{2L}, \tag{S65}$$

where $n_x = n_y = N$, thus circumscribing the square spatial frequency confine by the circular spatial frequency support.

In practice, when the spatial frequency support is indeed square, neither of these NA-equivalents are accurate. However, as the spatial frequency confine approaches the physical constraint of the back-aperture and invalid frequencies are physically rejected, or if we were to use a circular spatial frequency confine with diameter N, then $\mathrm{NA}_{\mathrm{eq,min}}$ would be accurate. Hence, we choose to compare resolution measures in our YPFM microscope against similar resolution measures in a widefield microscope equipped with an imaging objective of NA described by Eq. (S64).

In widefield microscopy, a point emitter (positioned in the focal plane) is imaged as an Airy disk with a FWHM closely approximated by the equation[12]

$$\mathrm{FWHM}_{\mathrm{Airy}} = \frac{0.51\,\lambda_{\mathrm{em}}}{\mathrm{NA}} \tag{S66}$$

where λ_{em} is the wavelength of emitted light (in vacuum), and NA is the numerical aperture of the imaging objective. To enable a comparison of $\mathrm{FWHM}_{\mathrm{YPFM,sim}}$ against the commonly used resolution measure $\mathrm{FWHM}_{\mathrm{Airy}}$, we combine Eq. (S64) with Eq. (S66), accepting the two approximations $2 \times (0.51) \approx 1$ and $\lambda_{\mathrm{em}} \approx \lambda$. This yields

$$\mathrm{FWHM}_{\mathrm{Airy}} \approx \frac{0.51\,\lambda_{\mathrm{em}}}{\mathrm{NA}_{\mathrm{eq,min}}} \approx \frac{L}{N}. \tag{S67}$$

A comparison of Eq. (S61) and Eq. (S67) reveals that we can expect the FWHM-resolution measure to be ~1.8 times better in our YPFM microscope when comparing it against an NA-equivalent widefield microscope. This prediction aligns with estimates presented in the main text.

In widefield microscopy, imaging resolution may also be quantified as the minimum distance ($\Delta_{\mathrm{Rayleigh}}$) between two identical point emitters required to satisfy the Rayleigh resolution criterion.

$$\Delta_{\mathrm{Rayleigh}} = \frac{0.61\,\lambda_{\mathrm{em}}}{\mathrm{NA}} \approx \frac{0.61\,\lambda}{\mathrm{NA}_{\mathrm{eq,min}}} \approx 1.22\,\frac{L}{\mathrm{N}}. \tag{S68}$$

When two identical point emitters, separated by $\Delta_{\mathrm{Rayleigh}}$ are imaged in a widefield microscope, they will satisfy the Rayleigh resolution criterion by forming an image (a superposition of two Airy disks) with a saddle-to-peak ratio of 0.735 (Born & Wolf[13], p. 597). This corresponds to a trough-to-peak ratio (i.e., contrast) of 0.265. As schematized in **Supplementary Fig. 5**, we used numerical simulations of Eq. (S57) to estimate the distance between two point emitters (imaged in our YPFM microscope) required to obtain a contrast of 0.265. By comparing results from these simulations against the NA-equivalent $\Delta_{\mathrm{Rayleigh}}$ in Eq. (S68), we found that our YPFM microscope will perform ~1.64 times better than widefield microscopy, when we quantify resolution in terms of the Rayleigh resolution criterion.

Supplementary Note 5
Probe pattern calibration and characterization

5.1 Calibrating the YPFM microscope

To run an YPFM image acquisition sequence in practice, we must imprint probe patterns with well-defined phase and spatial frequencies. Therefore, we must prior to imaging establish: #1 The relationship between the control voltage written to the delay stage and the phase ϕ of the probe pattern, and #2 The relationship between control voltages written to the galvanometric mirrors and the spatial frequencies (k_x, k_y) of the probe pattern.

To observe the probe pattern indirectly, we introduce a thin homogenously fluorescent sample (Alexa Fluor 568 carboxylic acid [A33081, Invitrogen] dissolved in PBS with at 35 μM) in the sample plane. When we imprint a given probe pattern onto this sample, the resulting fluorescence distribution captured with the sample-conjugate camera corresponds to an xy-cross-section of the probe pattern, i.e., the spatial distribution of excitation light intensity in the sample plane modulated by the quasi-Gaussian envelope function. To characterize probe patterns imaged in this way, we fit a 2D sinusoidal function and extract the fitted phase and spatial frequencies. As detailed in the following, we used a series of such fits to estimate relevant calibration coefficients. This was done with a custom-made calibration routine implemented in MATLAB (R2018b, The MathWorks, Inc.).

5.2 Calibrating the delay stage (phase of the probe pattern)

When calibrating the delay stage, we chart the relationship between the control voltage U_ϕ written to the delay stage and the phase ϕ of the probe pattern. Using the camera, we image a series of probe patterns while gradually increasing the control voltage across an observed phase-range of approximately 2.5π rad, i.e., slightly more than a full oscillation. Next, we extract the phase of the most prominent spatial frequency component in each image. Finally, we use a linear regression of the data points (ϕ, U_ϕ) to estimate a scalar conversion coefficient c, allowing us to imprint probe patterns with well-defined phase through Eq. (S69).

$$U_\phi = c\phi \tag{S69}$$

5.3 Calibrating the galvanometric mirrors (spatial frequencies of the probe pattern)

When calibrating the galvanometric mirrors, we chart the relationship between the four control voltages $(U_{M1}, U_{M2}, U_{M3}, U_{M4})$ written to the four galvanometric mirrors and the spatial frequencies (k_x, k_y) of the probe pattern. First, we manually adjust the control voltages such that the two beams approximately overlap, yielding a calibration image of the probe pattern with spatial frequencies near zero. Next, we image a series of probe patterns while gradually adjusting the control voltages across a two-dimensional range of spatial frequencies, roughly equivalent to the range of spatial frequencies used later during imaging. To deflect the laser beams symmetrically about the center of the objective back aperture, we always write the same voltages to the two horizontally deflecting mirrors ($U_{M1} = U_{M3} = U_{M13}$) and the two vertically deflecting mirrors ($U_{M2} = U_{M4} = U_{M24}$) respectively. As such, we treat the four control voltages simply as two control voltages (U_{M13} and U_{M24}). We extract the most prominent spatial frequencies of each imaged probe pattern, thus obtaining the data point $(k_x, k_y, U_{M13}, U_{M24})$ for each probe pattern. Finally, we use linear regression to obtain six calibration coefficients in matrix/vector form, allowing computation of control voltages required to imprint probe patterns with well-defined spatial frequencies through Eq. (S70),

$$\begin{bmatrix} U_{M13} \\ U_{M24} \end{bmatrix} = \begin{bmatrix} a_{1,1} & a_{1,2} \\ a_{2,1} & a_{2,2} \end{bmatrix} \begin{bmatrix} k_x \\ k_y \end{bmatrix} + \begin{bmatrix} b_1 \\ b_2 \end{bmatrix}. \tag{S70}$$

In practice, we captured a series of 1681 (41×41) images of the probe pattern, while covering a range of frequencies up to approximately 20 oscillations across the FOV ($L = 52$ μm). By analyzing these images, we estimated the six calibration coefficients presented in Eq. (S70). We obtained relatively low values of the non-diagonal elements ($a_{1,2}$ and $a_{2,1}$ < 0.6 % of $a_{1,1}$ and $a_{2,2}$) in the square 2-by-2 matrix, signifying a relatively low level of crosstalk. This means that in our instrument the spatial frequency along the x-axis is controlled primarily, albeit not exclusively, by the horizontally deflecting mirrors (controlled by U_{M13}), and similarly for the y-axis and vertically deflecting mirrors (controlled by U_{M24}).

5.4 Characterizing the quasi-Gaussian envelope function

The derivations presented herein assume that all probe patterns may be modeled as sinusoidal interference patterns modulated by $g(x, y)$, i.e., a spatial frequency-independent, quasi-Gaussian envelope function. Data presented in **Supplementary Fig. 6**, supports the validity of this assumption. Specifically, we used the camera to image a thin homogenously fluorescent sample (Alexa Fluor 568 in PBS), positioned in the sample plane, while imprinting a series of probe patterns within the spatial frequency confine $N = 60$. As exemplified in **Supplementary Fig. 6a**, a 2D image of the quasi-Gaussian envelope function was produced as the summation of probe patterns with four different phase-shifts, allowing to fit a 2D Gaussian function with five free parameters: x- and y-coordinates for the center, FWHM, magnitude, and offset. As summarized in **Supplementary Fig. 6b**, we found that the center coordinates of the quasi-Gaussian envelope were relatively stable, moving maximally ±3 μm across the 52 μm FOV. Similarly, the FWHM, magnitude and offset exhibited relative standard deviations of only ±1.42 %, ±1.84 %, and ±0.21 % of their respective averages.

Supplementary Note 6
YPFM is robust against long-term phase drift

6.1 Mathematical description of long-term phase drift in the YPFM microscope

In our YPFM microscope, the two beams propagate independently across relatively long distances (>0.5 m) before they combine and finally intersect to imprint an interference pattern on the sample. Slight temperature changes can cause asymmetric contractions/expansions of the two separate beam paths, manifesting as a temporal drift in the phase of the interference pattern. It is natural to assume that this phase drift would deteriorate image quality considerably. However, this is not the case – at least, when the phase drift is much slower than the image data acquisition time. For brevity, the following proof uses apostrophized variables and equation indexes matching the variables and indexes used in our previous derivations, which did not account for phase drift.

We modify Eq. (S9) into Eq. (S9') by introducing a new term, φ_{drift}, to our definition of the phase, ${\varphi_2}'$, of the complex electric field that describes one of the two beams transecting the sample. This new term represents an arbitrary phase shift induced by temporal drift of the imaging system. We assume that the rate of phase drift is slow and treat φ_{drift} as a constant in the context of capturing data to synthesize a single image,

$$ {\varphi_2}' = \mathbf{k_2} \cdot \mathbf{r} + \varphi_{02} + \varphi_{drift}. \tag{S9'} $$

Following the derivation presented in **Supplementary Note 2**, we can express the phase-shifted probe pattern, $I(x,y)'$, as

$$ I(x,y)' = I_0\, g(x,y)\left\{1 + \cos\left[x k_x(n_x) + y k_y(n_y) + \phi'\right]\right\}, \tag{S30'} $$

with

$$ \begin{aligned} \phi' &= \varphi_{02} + \varphi_{drift} - \varphi_{01} \\ &= \phi + \varphi_{drift}, \end{aligned} \tag{S33'} $$

where ϕ' is the new phase of the probe pattern.

Following the derivation presented in **Supplementary Note 3**, the four probe patterns imprinted during acquisition of a single complex Fourier coefficient, $\hat{c}(n_x, n_y)'$, now assume the form

$$ I(x,y,n_x,n_y,\phi = 0)' = I_0\, g(x,y)\left\{1 + \cos\left[x k_x(n_x) + y k_y(n_y) + \varphi_{drift}\right]\right\}, \tag{S41'} $$

$$ I(x,y,n_x,n_y,\phi = \pi/2)' = I_0\, g(x,y)\left\{1 - \sin\left[x k_x(n_x) + y k_y(n_y) + \varphi_{drift}\right]\right\}, \tag{S42'} $$

$$ I(x,y,n_x,n_y,\phi = \pi)' = I_0\, g(x,y)\left\{1 - \cos\left[x k_x(n_x) + y k_y(n_y) + \varphi_{drift}\right]\right\}, \tag{S43'} $$

$$ I(x,y,n_x,n_y,\phi = 3\pi/2)' = I_0\, g(x,y)\left\{1 + \sin\left[x k_x(n_x) + y k_y(n_y) + \varphi_{drift}\right]\right\}. \tag{S44'} $$

We note that φ_{drift} is independent of x and y. Therefore, we can move the drift term outside the integrals presented in Eq. (S51) and Eq. (S52), obtaining

$$\frac{1}{2I_0}\{[S(n_x,n_y,0)' - S(n_x,n_y,\pi)'] + i[S(n_x,n_y,\pi/2)' - S(n_x,n_y,3\pi/2)']\}$$
$$= \int_{-L/2}^{L/2}\int_{-L/2}^{L/2} f_{\downarrow z}(x,y)\; g(x,y)\{\cos[xk_x(n_x) + yk_y(n_y) + \varphi_{drift}] - i\sin[xk_x(n_x) + yk_y(n_y) + \varphi_{drift}]\}\; \mathrm{d}y\, \mathrm{d}x$$
$$= \int_{-L/2}^{L/2}\int_{-L/2}^{L/2} f_{\downarrow z}(x,y) g(x,y) \mathrm{e}^{-i[xk_x(n_x)+yk_y(n_y)+\varphi_{drift}]}\; \mathrm{d}y\, \mathrm{d}x$$
$$= \mathrm{e}^{-i\varphi_{drift}} \int_{-L/2}^{L/2}\int_{-L/2}^{L/2} f_{\downarrow z}(x,y) g(x,y) \mathrm{e}^{-i[xk_x(n_x)+yk_y(n_y)]}\; \mathrm{d}y\, \mathrm{d}x, \qquad \text{(S52′)}$$

where $S(n_x, n_y, \phi)'$ are signals measured with the single-element detector, as described in Eq. (S40).

By substituting Eq. (S52′) into Eq. (S37), we can express the complex Fourier coefficient, $\hat{c}(n_x, n_y)'$, obtained with the arbitrary phase drift, φ_{drift}. Next, by substituting from Eq. (S37), we can see that the phase drift merely rotates the phase of the estimated complex Fourier coefficient,

$$\hat{c}(n_x,n_y)' = \mathrm{e}^{i\varphi_{drift}} \frac{1}{2I_0L^2}\{[S(n_x,n_y,0) - S(n_x,n_y,\pi)] + i[S(n_x,n_y,\pi/2) - S(n_x,n_y,3\pi/2)]\}$$
$$= \mathrm{e}^{i\varphi_{drift}} \hat{c}(n_x,n_y). \qquad \text{(S53′)}$$

We note that φ_{drift} is independent of n_x and n_y, i.e., φ_{drift} does not change during acquisition of Fourier coefficients across all (n_x, n_y)-coordinates within the spatial frequency confine. This allows us to move the drift term outside the discrete sums presented in Eq. (S56). Finally, as $|\mathrm{e}^{i\varphi_{drift}}| = 1$, we can prove that YPFM images obtained with and without phase drift are equivalent.

$$\left|\widetilde{\Omega}_{\downarrow z}^{N}(m_x,m_y)'\right| = \left|\sum_{n_x=-N}^{N}\sum_{n_y=-N}^{N} \mathrm{e}^{i\varphi_{drift}} \hat{c}(n_x,n_y)\, e^{-i\pi(n_x+n_y)}\, e^{\frac{i\pi(n_x+n_y)}{M}}\, e^{\frac{i2\pi(n_xm_x+n_ym_y)}{M}}\right|$$
$$= \left|\mathrm{e}^{i\varphi_{drift}} \widetilde{\Omega}_{\downarrow z}^{N}(m_x,m_y)\right|$$
$$= \left|\mathrm{e}^{i\varphi_{drift}}\right| \left|\widetilde{\Omega}_{\downarrow z}^{N}(m_x,m_y)\right|$$
$$= \left|\widetilde{\Omega}_{\downarrow z}^{N}(m_x,m_y)\right| \qquad \text{(S56′)}$$

6.2 Experimental demonstration of robustness against phase drift

As summarized in **Supplementary Fig. 7**, we experimentally characterized the phase drift in our YPFM microscope and its impact on image quality. First, to gauge the rate of phase drift, we imaged a homogenously fluorescent sample while continuously imprinting a probe pattern with settings $n_x = 10, n_y = 0$. We captured a widefield image every 20 s, while keeping control voltages to the galvanometric mirrors and the delay stage constant. For each image, we estimated the phase of the probe pattern. As shown in **Supplementary Fig. 7a**, the resulting plot of phase versus time reveal that the phase of the probe pattern drifts smoothly at a rate that can exceed $\pi/4$ rad h^{-1}. We assume that this drift is caused by thermal fluctuations around the microscope, e.g., heating induced by laser radiation, heating conducted from instruments affixed to the metallic optical table, or convection upon opening/closing of the door to the laboratory. Our YPFM microscope is built in a laboratory with temperature control (active cooling and heating) designed to keep the room temperature within ±2 °C of the setpoint. It is reasonable to expect similar, or better, temperature control in other laboratories used for routine imaging. Finally, we captured multiple YPFM images of the same constellation of fluorescent beads. As shown in **Supplementary Fig. 7b**, YPFM images captured with

1 h intervals are near-identical, despite the substantial phase drift that would accrue between acquisitions. These observations corroborate our derivations in the previous section: Long-term phase drift does not affect imaging performance.

References

1. Walther, C. G., Whitfield, R. & James, D. C. Importance of Interaction between Integrin and Actin Cytoskeleton in Suspension Adaptation of CHO cells. *Appl Biochem Biotechnol* **178**, 1286–1302 (2016).
2. Sabri, S. *et al.* Differential regulation of actin stress fiber assembly and proplatelet formation by α2β1 integrin and GPVI in human megakaryocytes. *Blood* **104**, 3117–3125 (2004).
3. Colin-York, H. *et al.* Cytoskeletal actin patterns shape mast cell activation. *Commun Biol* **2**, 93 (2019).
4. Duarte, M. F. *et al.* Single-pixel imaging via compressive sampling. *IEEE Signal Process Mag* **25**, 83–91 (2008).
5. Gibson, G. M., Johnson, S. D. & Padgett, M. J. Single-pixel imaging 12 years on: a review. *Opt Express* **28**, 28190 (2020).
6. Calisesi, G. *et al.* Compressed sensing in fluorescence microscopy. *Prog Biophys Mol Biol* **168**, 66–80 (2022).
7. Goda, K. & Jalali, B. Dispersive Fourier transformation for fast continuous single-shot measurements. *Nat Photonics* **7**, 102–112 (2013).
8. Hoebe, R. A. *et al.* Controlled light-exposure microscopy reduces photobleaching and phototoxicity in fluorescence live-cell imaging. *Nat Biotechnol* **25**, 249–253 (2007).
9. Kreyszig, Erwin., Kreyszig, Herbert. & Norminton, E. J. *Advanced Engineering Mathematics*. (John Wiley & Sons, 2011).
10. Zhang, Z., Ma, X. & Zhong, J. Single-pixel imaging by means of Fourier spectrum acquisition. *Nat Commun* **6**, (2015).
11. William H. Press, B. P. F. S. A. T. and W. T. *Numerical Recipes in FORTRAN 77: The Art of Scientific Computing*. (1992).
12. Booth, M. J. *Microscope Resolution Estimation and Normalised Coordinates*. (2020).
13. Born, M. & Wolf, E. *Principles of Optics*. (Cambridge University Press, 1999).